A Closer Look into Slickenlines: Deformation On and Under the surface

Daniel Ortega-Arroyo & Matej Pec

Department of Earth, Atmospheric, and Planetary Sciences, Massachusetts Institute of Technology, Cambridge, Massachusetts, 02139, USA

Corresponding author: Daniel Ortega-Arroyo (dortega@mit.edu)

Key Points:

· Fault surfaces exhibit a self-affine roughness with a non-Gaussian height distribution.

· Samples of the same fault surface exhibit significantly different fractal parameters.

· Nanoparticulate layers are common on all fault rocks regardless of lithology or tectonic setting

Key Words: fault mirror, slickenline, fault surface roughness, principal slip zone, nanograins

Abstract

Slickenlines are lineations thought to record slip motion and mechanical wear within shear fractures. Their formation mechanisms and effect on friction and fault rheology are poorly understood. We investigate natural slickenlines from strike-slip, normal, and low-angle detachment faults formed in volcanic, quarzitic, and mylonitized sedimentary lithologies, respectively. Slickenline surfaces exhibit non-Gaussian height distributions and anisotropic self-affine roughnesses with corresponding mean Hurst exponents in directions parallel--0.53±0.07-- and perpendicular --0.6±0.1-- to slip. However, there is a significant variability in the fractal roughness descriptors obtained from multiple hand samples per fault surface.

Microstructural analyses reveal that the principal slip surface is formed by a thin (100 µm) nanoparticulate- and phyllosilicate-rich layer, followed by a ~10 m thick layer of increased cohesion, wherein several smaller grains coalesce into bigger aggregates. These microstructures are present in most analyzed samples suggesting that they commonly form during fault slip regardless of lithology or tectonic setting.

Our results 1) suggest that deformation immediately adjacent to fault surfaces is energetic enough to comminute the rocks into nanometric grains and 2) highlight the intricacies of fault systems not fully captured by current models, which are likely to impact stress distributions and frictional responses along faults.

Plain Language Summary

Grooved, polished rock surfaces known as slickenlines are thought to record the motion on fault blocks. The processes involved in slickenline formation and

their effects on a fault's behavior are poorly understood. We study naturally formed slickenlines from three different faults with different rock compositions. Slickenline surfaces reveal that their heights do not follow a normal distribution and that their surface textures have similar patterns over a wide range of scales of observations that are directionally-dependent with respect to the grooves.

Microscopic observations show that most of the deformation within our samples is usually concentrated within a narrow region (<100 µm) near the slickenline surface. This region is mostly composed of ultra-fine particles (<1 µm), micas and clay minerals, and glassy-like material. Our results suggest that a fault can release enough energy to break the rocks into nano-metric-sized particles during slip. Further, our results highlight additional textural information of the surface which impact how stress is distributed along faults and consequently how faults slip.

1. Introduction

Fault geometry has been shown to be a major factor contributing to earthquake rupture nucleation, propagation and arrest (e.g., Cattania & Segall, 2021; Sagy & Lyakhovsky, 2019; Scholz, 2019). The irregularities on the surface geometry, known as roughness, exert a direct control on surface properties that control many surface interactions such as real area of contact, friction, wear, and lubrication (e.g., Bhushan, 2013; Bowden et al., 1939; Dieterich & Kilgore, 1996).

Over the last decades, studies have shown that fault roughness exhibits a self-affine geometry that spans many scales of observation (e.g., Bistacchi et al., 2011; Candela et al., 2009, 2012; Power et al., 1987; Siman-Tov et al., 2015). A surface is a self-affine fractal if its different axes need to be scaled differently, i.e., an affine transformation, in order to observe self-similarity (Mandelbrot, 1985). Due to current limitations of subsurface imaging techniques, most of our understanding of fault processes relies on the study of exhumed fault surfaces. Slickensides -- which are smooth, striated rock surfaces -- are features commonly found along fault exposures with a variety of kinematic indicators, such as slickenlines, which are thought to record motion and mechanical wear of faulted blocks parallel to the slip motion (e.g. Doblas, 1998; Fleuty, 1975; Petit, 1987),

Current fault zone models feature a zone of distributed fracturing with increasing intensity that culminates in a highly strained fault core characterized by an abundance of highly fractured and comminuted fault rocks (Caine et al., 1996; Chester & Logan, 1986; Faulkner et al., 2010). The architecture of fault zones is then generally described by: a) distribution and number of cores, b) width and intensity of fracturing within the damage zone, and c) distribution of subsidiary faults (Faulkner et al., 2010, 2011). These descriptions, while convenient, can obscure the understanding of the mechanisms responsible for the myriad of structures found within fault zones and the strain partitioning between them

(Childs et al., 2012; Kim et al., 2004). For example, it is unclear what role slickenlines play within the overall development of fault zones despite their pervasiveness in fault exposures; only few studies have focused on how these surface expression of faults relate to specific deformation processes (Ault et al., 2019; Houser et al., 2021; Ohl et al., 2020; Power & Tullis, 1989; Rowe et al., 2019; Siman-Tov et al., 2015; Toy et al., 2017; Verberne et al., 2014, 2019).

Similarly, despite the success of rate and state friction (RSF) in characterizing laboratory friction experiments, e.g., velocity-stepping tests, RSF provides little physical basis that would allow successful extrapolation of such results to the scales and conditions of natural faults. In depth study of fault surfaces and their respective rock volume is thus essential to better understand the microphysical processes involved in the deformation along faults (Chen et al., 2020; van den Ende et al., 2018). For instance, it is now understood that a variety of mechanisms occurring throughout the volume of rocks mediate their frictional response during deformation, including melting, (Magloughlin & Spray, 1992; Nielsen et al., 2010; Spray, 1992) amorphization (Houser et al., 2021; Kirkpatrick et al., 2013; Kuo et al., 2016; Ohl et al., 2020; Pec et al., 2012, 2016; Pec & Al Nasser, 2021; Rowe et al., 2019; Verberne et al., 2019), crystal-plastic deformation (Bestmann et al., 2011; Chen et al., 2020), and nanoparticle formation (Bhushan, 2013; Di Toro et al., 2011; Ohl et al., 2020; Tisato et al., 2012; Verberne et al., 2014, 2019), among others.

Therefore, to identify the surface properties of faults and the dominant processes occurring during fault slip and slickenline development, we characterize the surface of slickenlines and study their microstructure in a number of lithologies in nature.

2 Methods

Hand samples of slickenline surfaces were taken from 3 different fault systems--a right lateral Falla de Plan de los Plátanos fault (PP) in SE Jalisco, Mexico, the Big Piute Ranges low angle normal fault (BP), and Waterman Hills detachment fault (WH), both in SE California-- that represent different lithologies and/or tectonic settings, Fig. 1. At each locality, we aimed to sample specimens that preserved both sides of the fault surface, if possible, to better capture the structures and materials that comprise slickenlines. The faults--PP, BP, and WH--cut through andesite, quartzite, and mylonitized metasedimentary (*MMS*) rocks, respectively.

2.1 Sample preparation

The collected hand samples (1 from PP, 2 from BP and 2 from WH) were cleaned of any loose debris and dirt prior to any surface measurement. Portions of the samples were then prepared for thin sections with the observable surface perpendicular to the plane of the slickenline slip surface. Using Tikoff et al. (2019) naming convention, *XZ* and *YZ* correspond to thin sections oriented

parallel and perpendicular to the slip lineations, respectively.

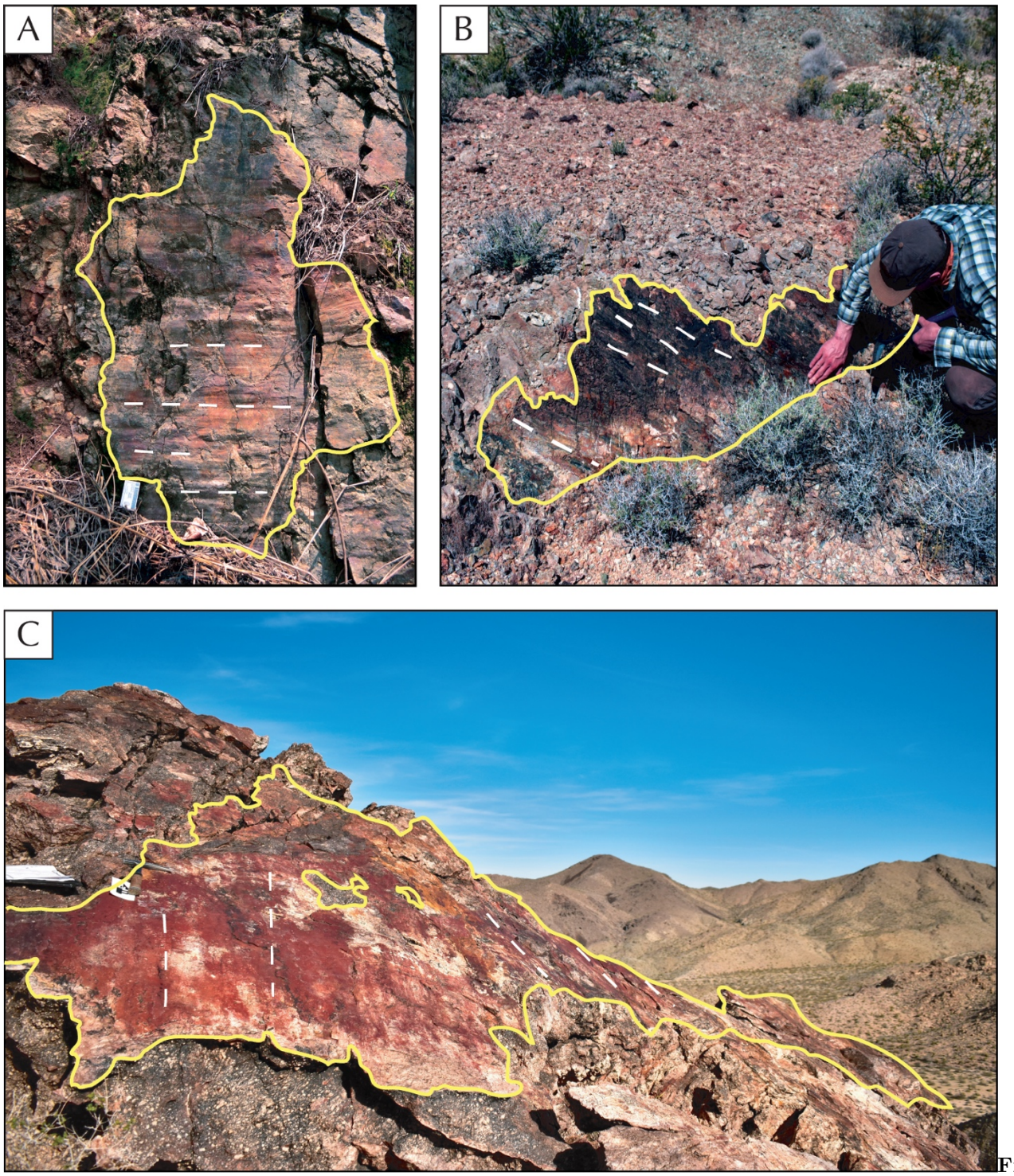

Fi

1. Sampled fault surfaces. A) Slickenlines at the right lateral strike-slip, Falla de Plan de Plátanos, ID card for scale. White dotted lines indicate slip lineations. B) Minor slip surface cutting through the mylonitized footwall of the WH. C) Subsidiary fault within the BP fault damage zone.

2.2 Roughness analysis

We characterized and quantified the slickenline roughness of the different fault surfaces over six orders of magnitude ranging from 100's of nm to 3 cm. Each surface (between 100 mm^2 to 1000 mm^2) was measured by a Taylor Hobson TALYSCAN 150 profilometer using a no-contact laser gauge with a 252 nm vertical resolution. A constant 2 mm s^{-1} traversing speed and a 5 µm spacing were used for each measurement unless otherwise indicated.

At the micron scale, the slip surfaces' topography was measured by manually tracing the surface profile of selected thin sections imaged through Secondary Electron Microscopy (SEM).

2.2.1 Hurst Exponent Estimation

The TALYSCAN 150 measurements were processed in Matlab to remove any planar inclination trend associated with the initial sample placement on the profilometer. 1) The measurements- in the form of an elevation matrix- are then rotated such that the horizontal axis (x-axis) of the 3D and digital elevation models (DEM) are parallel to the slip lineations. Once the trend has been removed from the elevation matrices, we proceeded to calculate the Hurst exponent using power spectrum density analyses (PSD), Fig. 2, (c.f., Bistacchi et al., 2011; Candela et al., 2009, 2012; Jacobs et al., 2017; Siman-Tov et al., 2013). 2) Profiles parallel and perpendicular to the slip lineations are extracted from each surface. A one-dimensional Hann window function is then applied to each line scan to correct for measurement artifacts, particularly near the edges, as suggested by Jacobs et al. (2017). 3) The Fourier power spectrum $P(k)$ is calculated for each profile as a function of wavenumber (k) and normalized by dividing the power spectrum by the length of the corresponding profile. 4) The power spectra for both the parallel and perpendicular directions to slip are averaged at each wavenumber to reduce noise associated with each individual profile. 5) The Hurst exponent is then estimated from the best fit to a power-law of the form $P(k)=Ck^{1-2H}$,

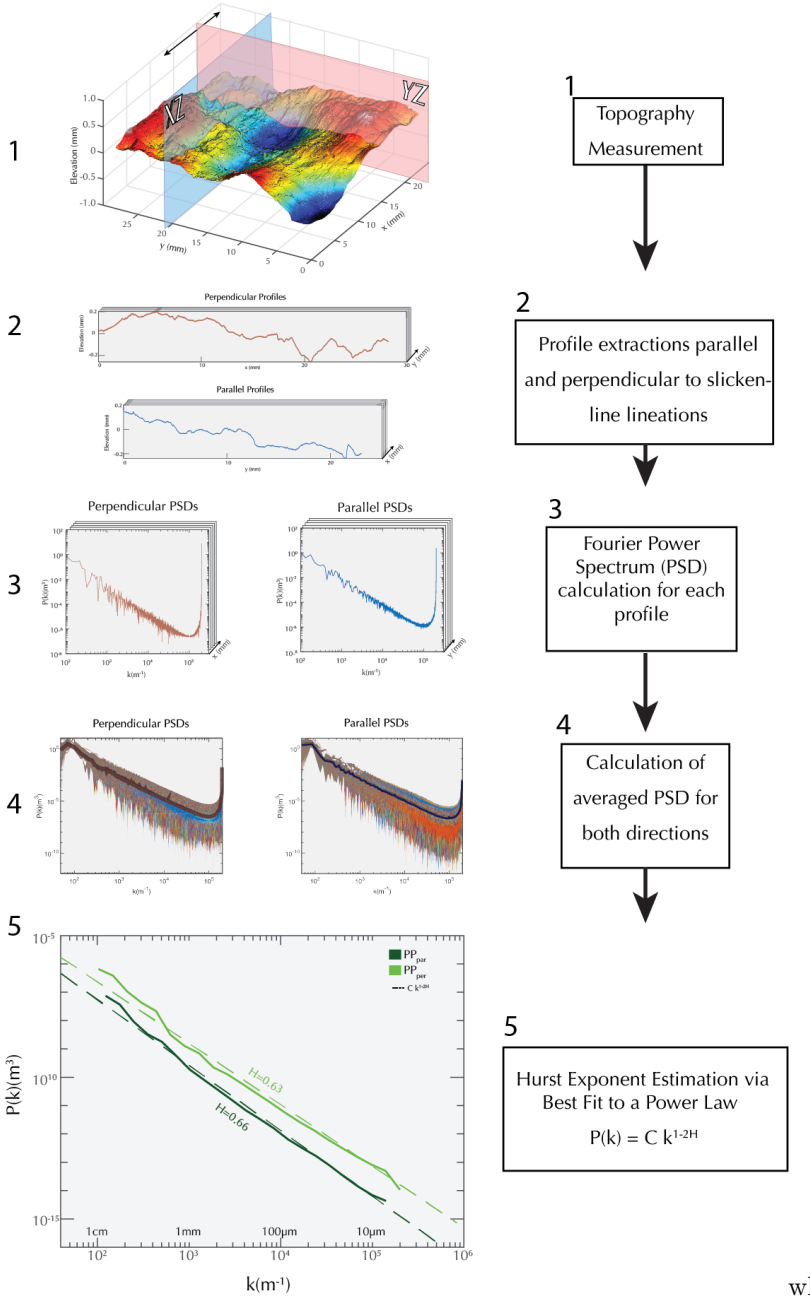

where H is the Hurst exponent, and C is the pre-factor. The workflow is illustrated in Fig. 2.

Figure 2. Calculation of Hurst Exponent. See text for details.

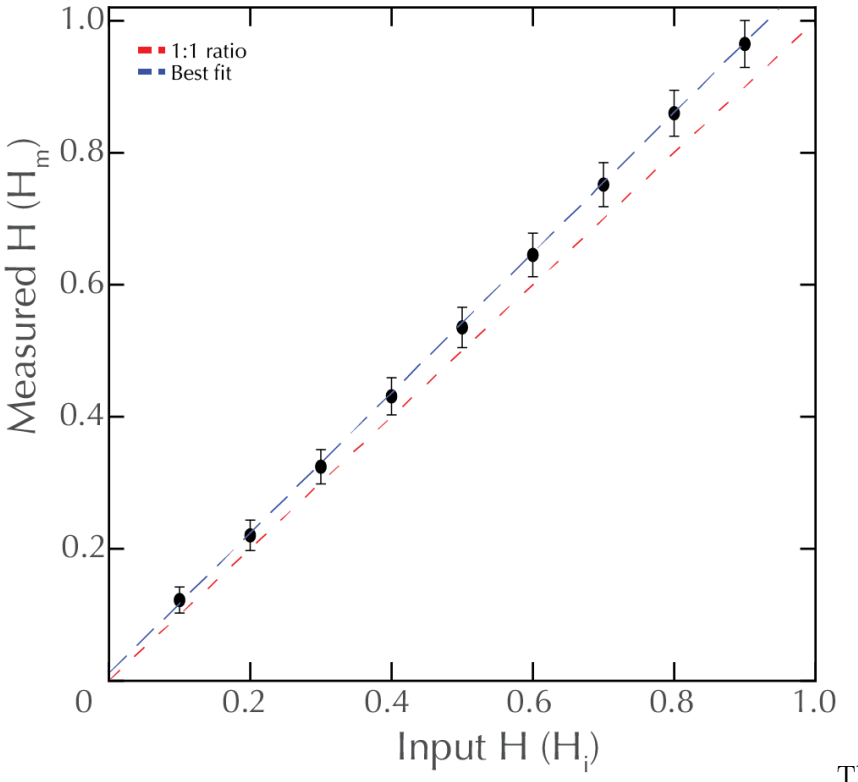

The accuracy of the signal processing technique was assessed by recording the difference between the "input" Hurst exponents of randomly generated synthetic isotropic self-affine surfaces using the code provided in Candela et al. (2009) and the "output" recovered with our methods. For each value of the input Hurst exponent, we analyzed a set of 1000 synthetically generated surfaces as presented in Fig. 3. We further assessed our method by analyzing surface data from the Corona Heights fault surface samples from Thom et al. (2017). The average Hurst exponents of the Corona Heights Fault slickenline samples corresponded to 0.72 ±. 0.11 and 0.78 ± 0.09 for the parallel and perpendicular orientations, respectively. However, when the data in both directions are taken into account, we obtained 0.75 ± 0.10, which agrees with the value found by Thom et al. (2017).

Figure 3. Calibration of PSD method for calculating the Hurst exponent (*H)*. Note that the measured Hurst exponent (H_m) does not follow a one-to-one ratio (red). Instead, it has a linear best fit of the form H_m=*1.065* H_i *+ 0.006* with a coefficient of determination R^2=0.999.

2.2.2 Multiresolutional Analysis

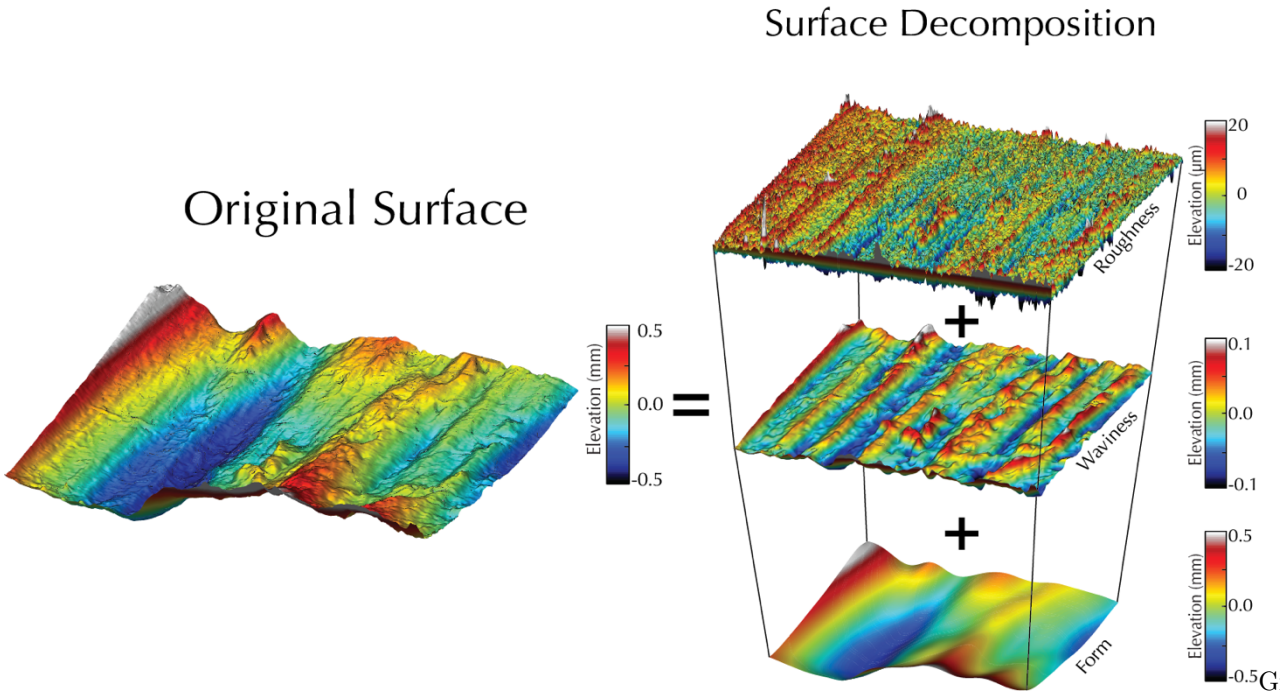

that the roughness measurements are inherently a superposition of surface texture information from different length scales, we performed a multi-resolutional analysis (MRA) in addition to the Hurst exponent calculation. An MRA consists of decomposing the surface topography at various cutoff wavelengths to separate the surface texture into 1) *form*, 2) *waviness* (macro-roughness), and 3) *roughness* (micro-roughness) as shown in Fig. 4. We used a Gaussian 2D filter to separate the data into three different length scales with cut off wavelengths centered at 5 mm and 500 µm. Care is taken that the energy of the signal is preserved, i.e., that the original signal can be fully reconstructed when all components are added together. Furthermore, for each component, we calculate the kurtosis and skewness of the height distribution.

Figure 4. Schematic of a Multiresolutional Analysis shows how a surface measurement is decomposed into characteristic wavelengths.

2.3 Microstructural Analyses

We study a) the grain size distributions and b) the morphologies and cross-cutting relationships preserved in, and adjacent to, the slickenlines. We aim to identify the microphysical processes occurring within the slickenline volume.

2.3.1 Imaging conditions

Thin sections oriented parallel (XZ) and perpendicular (YZ) to the slip direction were analyzed using a ZEISS AX10 Petrographic microscope and ZEISS Merlin

HR-SEM equipped with a Backscattered electron (BSE) detector at the Department of Earth Atmospheric and Planetary Sciences and Materials Research Science and Engineering Centers at the Massachusetts Institute of Technology, respectively.

The SEM was operated with a beam current of 5 nA and a 15 kV accelerating voltage unless otherwise indicated. To better capture the range of structures and grain sizes, images were acquired at various magnifications resulting in a 0.77 nm/px to 2.06 µm/px resolution.

2.2.2 Grain Size analysis

Grain size measurements were obtained by manually tracing petrographic microscopy and BSE images obtained at progressively higher magnifications. At each magnification we trace the maximum number of discernible grains/clasts, typically 300-3000 segmented grains per image range are used. Segmented images were then imported to *ImageJ* to calculate the area (A) of each grain in pixels. Grains with areas smaller than 20 pixels were excluded. The size of each grain is then approximated by calculating the diameter of a circle with the same area. The equivalent diameters (d_{eq}) were calculated as

$$d_{\mathrm{eq}} = 2\sqrt{\frac{A}{\pi}}, \quad (1)$$

and collected in a histogram with ten bins for each magnification.

The bins from each magnification are plotted in a logarithmic scale to determine the slope (S_n) and intercept (I_n) of the best power-law fit. The frequency of each bin is then multiplied by a factor (L_n) that reflects the relative magnification at each image to correct for undercounting of the total number of grains from analyzing progressively smaller areas. The factor, L_n, is determined by:

$$L_n = 10^{I_{\max} - I_n}, \quad (2)$$

where $I_{\max}$ corresponds to the intercept of the lowest magnification. The results from all magnifications are then combined into a single plot.

3. Results

3.1 Roughness Analysis

To constrain the surface properties of the samples related to their geometry, we performed roughness analysis. These include calculation of the Hurst exponent and morphological and statistical descriptions of the surface texture and height distribution.

In Figure 5 we show the wide variety of surface textures that can be qualitatively grouped into two general domains, "*smooth*" and "*rough*", based on the amplitudes and frequency of the dominant asperities.

3.1.1 Power Spectral Density Results

The averaged power spectral density (PSD) curves for all roughness measurements are shown in Fig. 6. PSDs are obtained from profiles scanned parallel (*par*) and perpendicular (*per*) to the slip lineations, i.e., the x- and y-directions, as illustrated in Fig.2.

Spectra for most measurements show only limited variability in the slope of profiles measured parallel to lineations with a mean Hurst exponent of 0.53 $\pm$ 0.07 and a range of 0.41-0.63. In contrast, the perpendicular profiles showed a wider variability with values of H_{per} ranging from 0.45-0.72 and a mean of 0.60 $\pm$ 0.10. The pre-factor (C) is directly proportional to root mean squared roughness (RMS) by

$$\mathrm{RMS} = \sqrt{\left[\frac{\mathrm{Ck}^{-2\mathrm{H}}}{-2\mathrm{H}}\right]_{\mathrm{k_{min}}}^{\mathrm{k_{max}}}} \quad (3)$$

And thus, a higher C indicates overall higher roughness amplitude, whereas a lower H indicates a larger contribution of smaller wavelengths/higher spatial frequency, i.e., relatively rougher at smaller length scales than a self-similar surface ($H = 1$) with the same C.

While the samples studied in this paper show a relationship between the pre-factors and H, the inclusion of measurements from Bistacchi et al., (2011) and Candela et al., (2013) indicates no clear trend, Fig 6B. Furthermore, measurements of the various hand samples obtained from the same fault surface show a wide range in both H and C values, Table 1.

-

Table 1. Hurst (H) and Pre-exponents (C)

@ >p(- 8) * >p(- 8) * >p(- 8) * >p(- 8) * >p(- 8) * @ **Fault** &

H_{par}

&

$\boldsymbol{H_{per}}$
&

$\boldsymbol{C_{par}}$
&

$\boldsymbol{C_{per}}$

Plan de Plátanos & & & &
& 0.61 & 0.58 & 2.5×10^{-3} & 2.2×10^{-3}
Big Piute & & & &
Min & 0.41 & 0.45 & 3.4×10^{-5} & 2.2×10^{-3}
Max & 0.52 & 0.72 & 2.2×10^{-3} & 1.8×10^{-2}
Waterman Hill & & & &
Min & 0.51 & 0.48 & 4.9×10^{-4} & 2.2×10^{-3}
Max & 0.65 & 0.71 & 3.5×10^{-2} & 6.2×10^{-2}

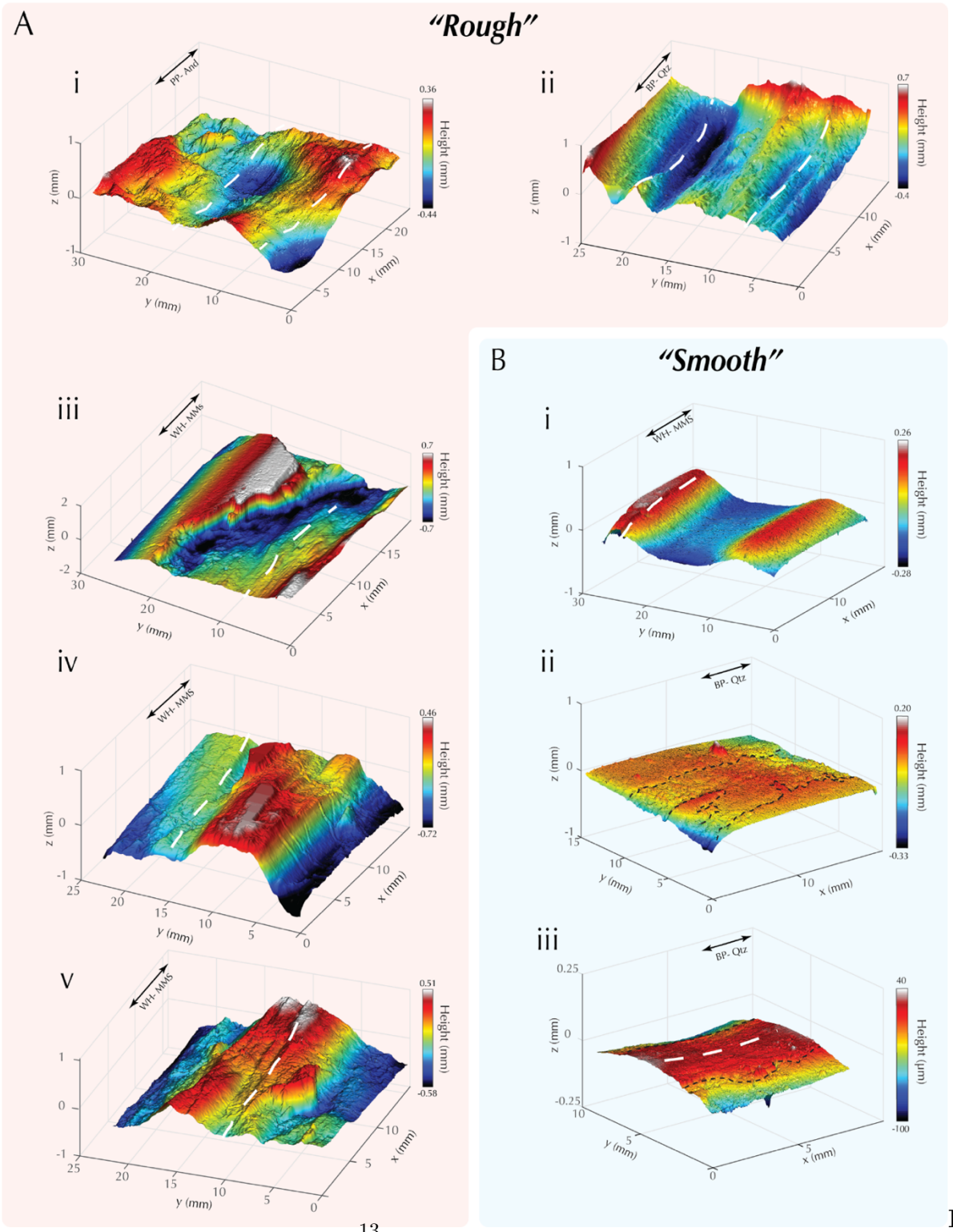

Figure 5. Topography of the different surfaces collected via laser profilometry qualitatively grouped in A) rough and B) smooth surfaces. White dotted lines highlight grooves and lineations. Black dotted lines highlight transitions in roughnesses. PP-, WH-, and BP- indicate the fault system, whereas And (andesite), MMS (mylonitized meta-sedimentary), and Qtz (quartzite)

Skewness (sk) and kurtosis (kur) are statistical measures that describe the symmetry and peakedness of the height distributions, e.g., a distribution is known as a gaussian when $sk=0$ and $kur=3$. A high kurtosis ($kur>3$) corresponds to a distribution with a greater peakedness than a gaussian, which indicates more height measurements are centered near the mean height, whereas the converse is true for a low kurtosis ($kur<3$). Furthermore, a positive and negative skewness indicates most measurements lie either below or above the mean surface, respectively, as illustrated in Fig. 7. The samples show a wide range of sk and kur values, with no systematic variation with respect to lithology or fault system. However, samples wherein lineations are more apparent and visually rougher tend to have more positive skewness. In contrast, kurtosis is generally higher for smoother samples.

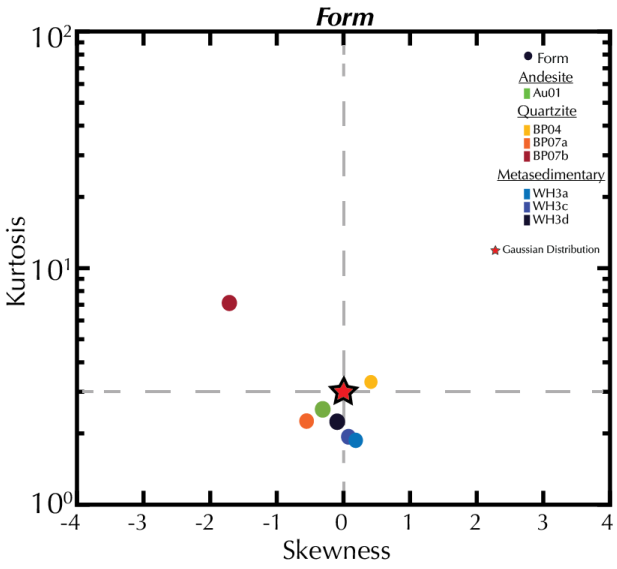
Form
Kurtosis
Skewness
Form
Andesite
Au01
Quartzite
BP04
BP07a
BP07b
Metasedimentary
WH3a
WH3c
WH3d
Gaussian Distribution

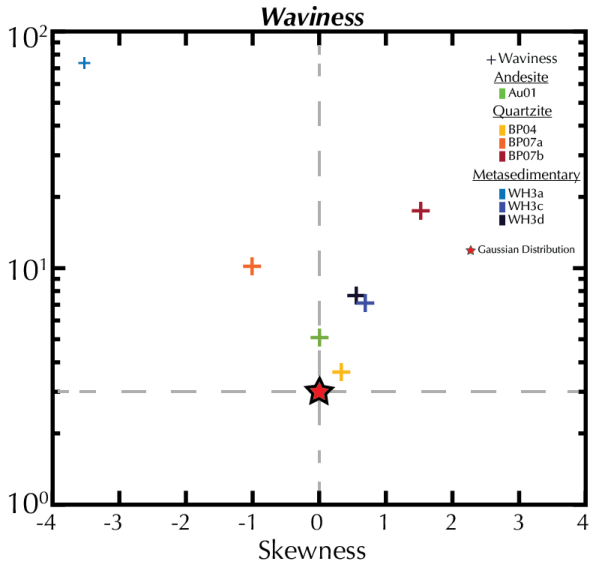
Waviness
Skewness
Waviness
Andesite
Au01
Quartzite
BP04
BP07a
BP07b
Metasedimentary
WH3a
WH3c
WH3d
Gaussian Distribution

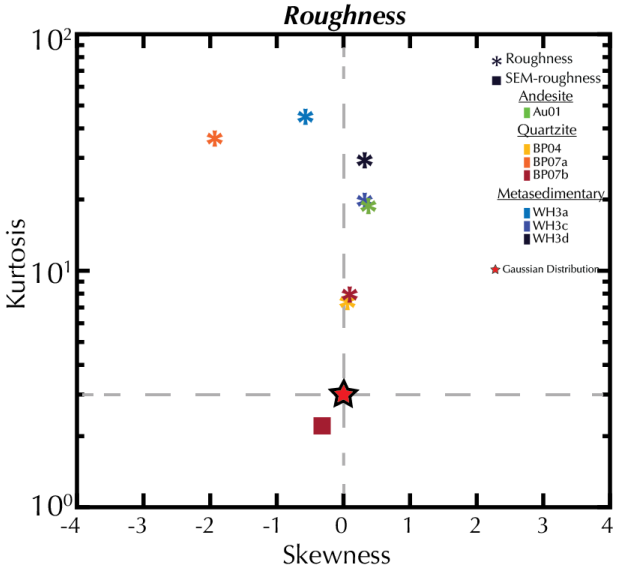
Roughness
Kurtosis
Skewness
Roughness
SEM-roughness
Andesite
Au01
Quartzite
BP04
BP07a
BP07b
Metasedimentary
WH3a
WH3c
WH3d
Gaussian Distribution

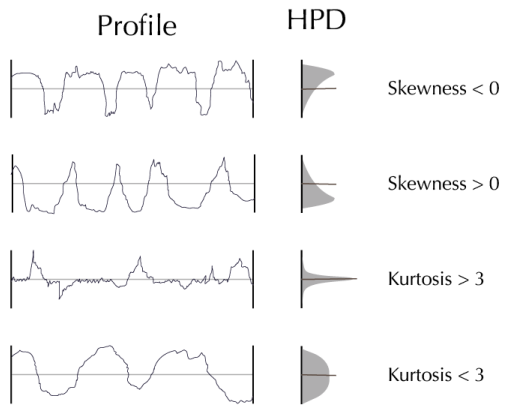
Profile
HPD
Skewness < 0
Skewness > 0
Kurtosis > 3
Kurtosis < 3

Figure 7. Skewness and kurtosis for samples A) *Form*, B) *Waviness*, and C) *Roughness*. D) Schematic surface profiles with positive and negative skewness and kurtosis values higher and lower than three.

3.2 Structural and Microstructural Observations

With the aim of interpreting the processes involved in fault slip and slickenline development, we selected representative samples from each locality to describe in greater detail. We focused on the morphologies at the surface and throughout the rock volume adjacent to the slip surface. For each sample, we specifically examine a) the size and spacing of the lineations, b) orientation of structures on the slip surface, c) the structures within the host rock immediately adjacent to the slip surface, and d) the grain size distribution.

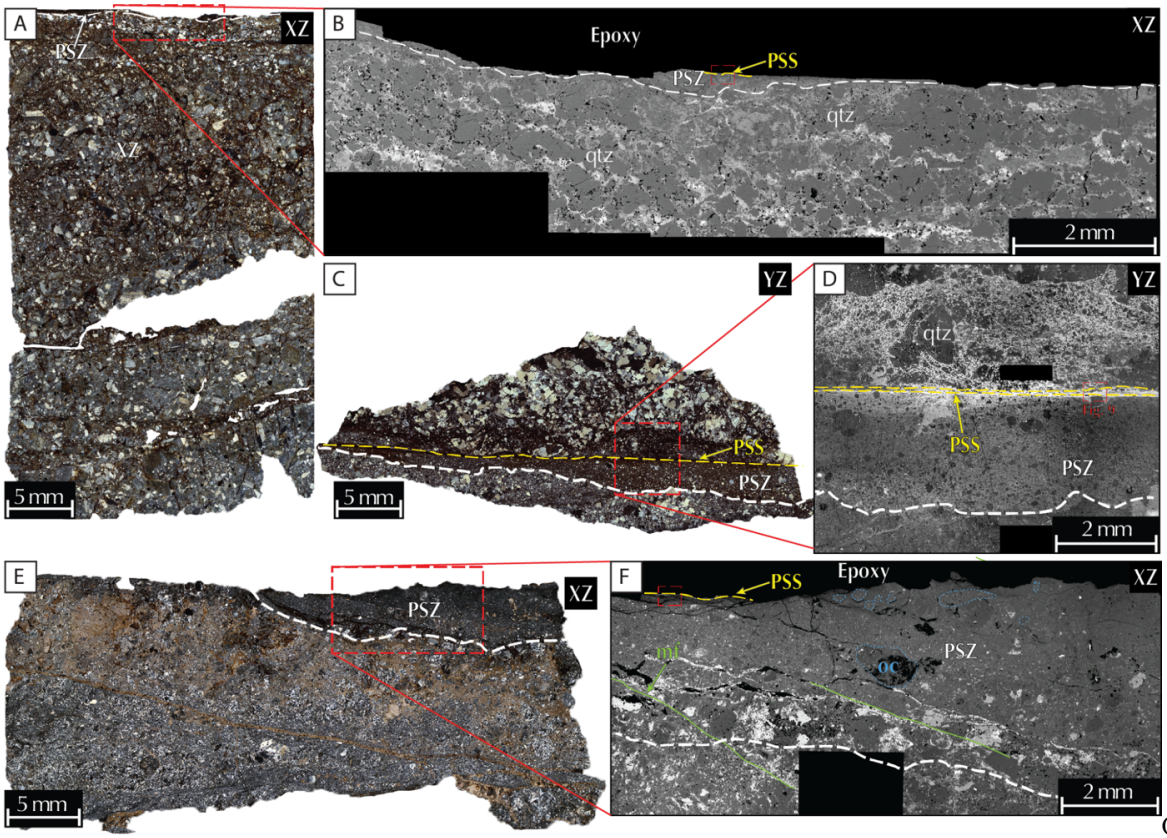

Given the lack of reliable strain markers in our samples to accurately determine slip displacements, we use the thickness of the cataclastic zone, length of lineations or groves (Brodsky et al., 2020), and the data presented in (Shipton et al., 2006) to make an order of magnitude estimate on the displacements likely

experienced by the faults

Figure 8. Selected samples for microstructural analysis. A) Andesite hosted slickenline thin sections under cross-polarized light (XPL). Note relatively undeformed primary igneous fabric at the bottom of the image. B) SEM-BSE close-up of A. White dashed lines highlight a Principal Slip Zone (PSZ) characterized as a zone of highly comminuted grains of irregular thickness. Dark grey colors correspond to quartz (qtz), whereas black spots within the rock volume correspond to porosity. Note *S-C* cataclasite with top to the left sense of shear. C) Quartzite hosted slickenlines under XPL, preserving opposing segments of the fault surface. D) SEM-BSE close up of C. Note the principal slip zone (PSZ) is characterized by highly comminuted grains in the m-size range, whereas the principal slip surface (PSS-yellow) is localized to few tens of microns and decorated by an abundance of Fe-oxide minerals (bright colors). Note asymmetry in Fe-oxide distribution and comminution between both sides of the fault. E) Mylonitized metasedimentary hosted slickenline under XPL. F) Close-up of E shows the presence of a Principal Slip Zone (PSZ) of variable thickness characterized by sharp grain size reduction towards the slip surface and towards a thin Principal Slip Surface (PSS). Note the presence of older cataclastic clasts (OC) within the PSZ. Micro-faults (mf-green) are also observed offsetting the PSZ.

3.2.1 Plan de los Plátanos Slickenlines

This sample was collected from a minor splay of the PP fault that likely accommodates tenths of centimeters of displacement NW of Autlán de Navarro, Jalisco, Mexico, on the side of the road near the town of Jalocote (De la Teja Segura & Roque Ayala, 2007). The host rock is a porphyritic andesite with sericitized plagioclase phenocrysts in the 0.1-1.0 mm range. The rock is heavily hydrothermally altered. Secondary epidote, chlorite, and iron oxides comprise the bulk of the groundmass closer to the slip surface. Despite the heavy alteration and hosting of slickenlines, the host rock seldom records pervasive/distributed deformation as the primary igneous texture is relatively intact a few cm away from the slip surface, Fig 8A.

The slip surface is covered by a thin translucent film that is glossy and smooth, with specularly reflective patches. The lineations have an average width of 527 $\pm$ 83 m and spacing of 0.85 $\pm$ 0.18 mm that remain relatively constant throughout the length of the sample Fig. 5A. Secondary fractures perpendicular and diagonal to the lineations cross-cut the surface.

Below the surface, we identified a quartz-rich vein with predominantly ductile fabrics that soles into the slip surface. The quartz grains are elongated, exhibit undulose extinction and host multiple inclusions. All fabrics are then cut by ~200 µm thick principal slip zone (PSZ) characterized by a sharp decrease in grain size from the host rock towards the slip surface, Fig. 8A-B.

The PSZ features a zone of increased cohesion (ICZ), Fig 9A, comprising grains

with serrated, interlocked grain boundaries, triple junctions, and coalescence of several smaller grains into bigger aggregates, and a ~5 µm thin principal slip surface (PSS). The PSS is characterized by a predominance of mostly rounded nm-size grains/particles, embedded within a matrix of phyllosilicates (ps) and possibly amorphous material (am?), Fig. 9B.

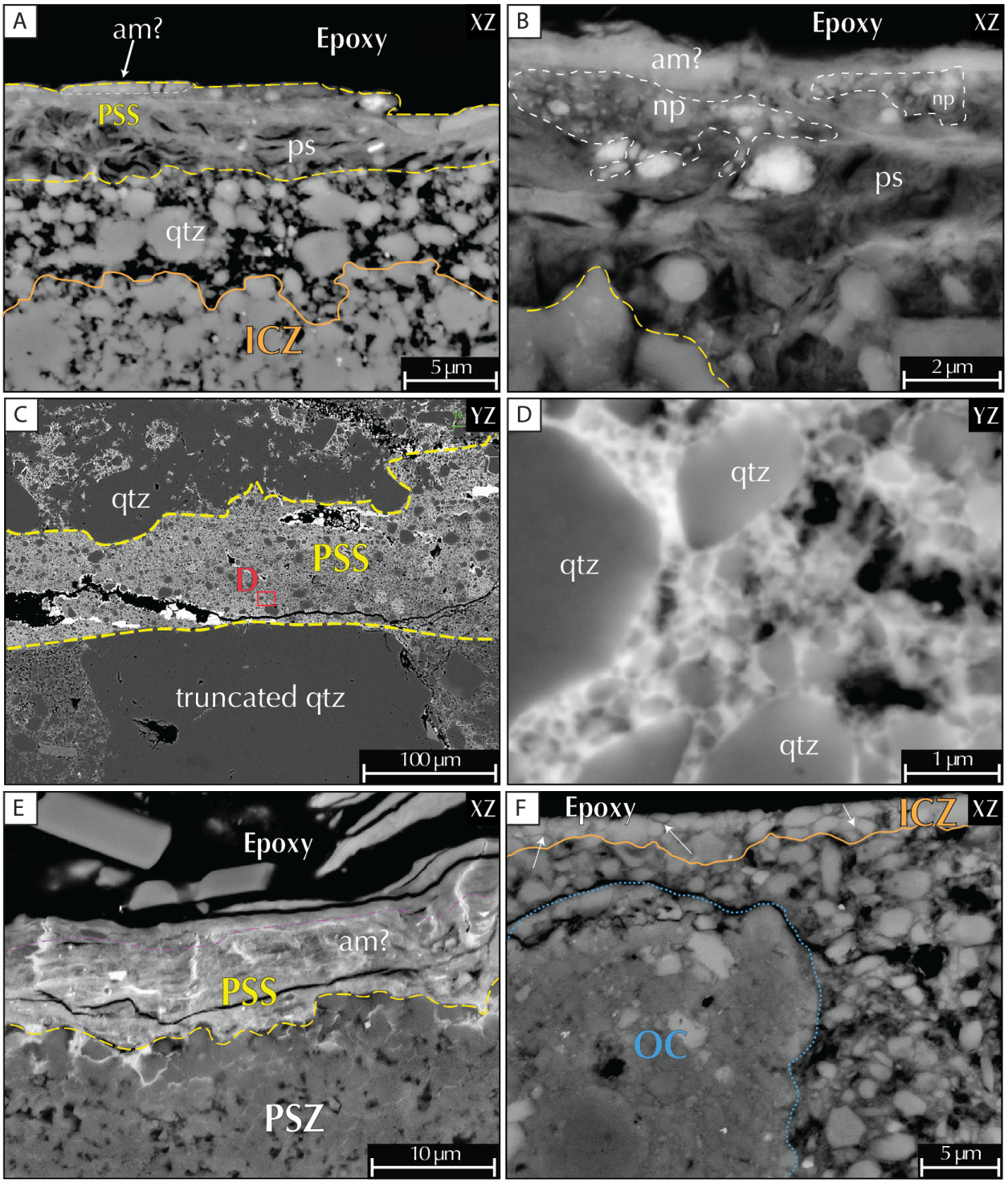
A
am?
Epoxy
XZ
PSS
ps
qtz
ICZ
5 µm
B
Epoxy
XZ
am?
np
np
ps
2 µm
C
YZ
qtz
PSS
D
truncated qtz
100 µm
D
YZ
qtz
qtz
qtz
1 µm
E
XZ
Epoxy
am?
PSS
PSZ
10 µm
F
Epoxy
ICZ
XZ
OC
5 µm

Figure 9. SEM-BSE images of the Principal Slip Zones. **Andesite hosted slickenlines:** A) Close up of PSZ in Fig 8B, showing the presence of a thin PSS and an Increased Cohesion Zone (ICZ) and PSS. Note the PSS is a thin layer (a few microns thick) comprising randomly oriented phyllosilicate (ps), a possibly amorphous material (am?), and nano-sized particles (np). The ICZ is separated from the PSS by a thin, relatively porous layer of nm- m sized grains. Note the roundness of most clasts. The ICZ is characterized by a decrease in porosity, grains with irregular and serrated grain boundaries, and sintering microstructures. B) Close up of PSS. Note the presence of rounded nano-sized particles (np) embedded in a phyllosilicate (ps)/possibly amorphous material (am?) matrix. **Quartzite hosted slickenlines:** C) Close up of the PSS. Image shows a sharp decrease in grain size from the PSZ (outside of the yellow boundary) towards the PSS, which is characterized by a Fe-oxide-rich layer of micron-sized grains supported in a fine grain matrix. Note truncation of quartz clast by the PSS. D) Close-up of PSS matrix shows matrix comprises predominantly nm-sized qtz grains and Fe-ox cement (bright colors). Note roundness and lack of fractures on matrix grains. **MMS hosted slickenlines:** E) Close up into the PSS shows it comprises a layered possibly amorphous phase (am?) with non-descript grain boundaries. Layering is highlighted by a magenta dotted line. F) Close up into the PSZ adjacent to the PSS shows an abundance of nm-sized particles (np) in the interstitial spaces of the larger (m-sized) grains. Note large, agglomerated clast with lower porosity (OC-blue) and an ICZ (orange) leading to the slip surface. Grains within the ICZ have their long sides preferentially oriented parallel to the surface and possess triple junctions (white arrows). Image taken at 20 kV and 10 nA.

3.2.2 Big Piute Slickenlines

Slickenlines from this location were collected from small subsidiary faults within the damage zone of the BP that likely accommodated no more than a few meters of displacement. Unlike the other samples, the slickenlines in these faults are hosted within a monomineralic quartzite host rock with a primary grain size ranging from 200 µm - 1 mm. The quartz grains within the host rock exhibit serrated grain boundaries, undulose extinction, deformation lamellae, and a shape preferred orientation (SPO) at ~45° degrees from the slip surface. Furthermore, the host rock is cut by through-going microfractures perpendicular to the SPO.

The slip surfaces are extremely flat and smooth, particularly in the *XZ* orientation. Iron-oxides (Fe-ox) decorate the slip surfaces, including botryoidal hematite. The lineations are marked by alternating thin Fe-ox bands with a spacing of 8.2 ± 0.5 mm and 1-3 mm wide grooves.

Areas in which portions of both sides of the fault surface are preserved, Fig. 8C-D and Fig. 9C-D, shows an asymmetric distribution of the deformation. A well-developed and distributed cataclasite that fines towards the slip surface characterizes the footwall. In contrast, a predominantly fractured and brecciated host rock that is abruptly cut by the slip surface comprises the bulk of

the hanging wall.

We observe a PSZ leading to the slip surface and a ~10 µm thick PSS. The PSS is characterized by truncation of grains from the PSZ, a matrix comprising rounded nanometric grains with little to no fractures and Fe-ox cement, and a predominantly nanometric unconsolidated fluidized gouge, Fig. 8C.

3.2.3 Waterman Hill Slickenlines

WH samples were collected from a minor fault exposure found within the mylonitized footwall of the Central Mojave Metamorphic Core Complex exposed along the Mitchell Range N of Barstow, SE California (see Fletcher et al., 1999). The fault surface occurs at the lithological boundary of gneissic and metacarbonate protoliths. The slickenlines are hosted within a thick cataclasite (larger than the hand samples) comprising multiple lithologies. The rock itself is overprinted by hydrothermal alteration and calcite-filled fractures, Fig. 8E-F.

The surface forms a resistant ledge, is smooth and specularly reflective. The lineations are marked by cm-scale undulations within mirror-polished regions and by 520 ± 160 µm wide grooves in unpolished portions of the surface.

We observe that the WH slickenlines also exhibit a region of extremely comminuted grains, PSZ, adjacent to the slip surface. Unlike the other samples, the PSZ here varies significantly in thickness, from ~100 µm to 5 mm, along the direction of slip (XZ). Regions where the PSZ is thicker exhibit numerous micro-faults that displace the PSZ but do not cross-cut the mirror-polished surface. The PSZ contains clasts of earlier, more consolidated cataclasites (OC). Immediately adjacent to the slip surface, two main features are prominent: a) the presence of a potentially amorphous coating within the PSS with no discernable grain boundaries and b) an ICZ where porosity is decreased and grains exhibit triple junctions and an SPO with their long axes preferentially aligned subparallel to the surface, Fig. 9E-F. Nanosized grains are also observed to be common within the matrix of the PSZ.

3.3 Grain Size Distribution

To characterize the comminution processes occurring during slip, we analyzed the grain size distribution of the fault rocks in the vicinity of the slip surface. Here we present the results of the grain size analyses performed on two sequences of petrographic microscopy and SEM images taken at increasing magnifications from selected samples from the BP and PP faults. The results are plotted on log-log plots of frequency vs. equivalent diameter to determine the grain size distribution (GSD) and presented in Fig. 10.

We did not perform grain size analysis on samples from the WH Fault. It was not possible to accurately identify individual grain boundaries as the particles appear embedded within a cement of similar composition. Furthermore, when the boundaries between particles could be accurately identified, they exhibit triple junctions, suggesting static crystal growth, and thus obscuring the grain sizes related to the comminution process.

The grain size distribution for the quartzite sample shows a power-law functional relationship over six orders of magnitude (10's nm-1's mm) with a constant slope *of D = 2.73 ± 0.05* despite the sharp decreases in grain size observed within the transition from the host rock towards the PSZ and PSS respectively, Fig. 9C-D. However, it is observed that at the lower grain size range (less than 100 nm), the distributions start to plateau as the grain size approaches the resolution limit of the SEM (a single pixel at the highest magnification equals 0.77 nm). The smallest grain sizes are found within the unconsolidated gouge with an equivalent d_{min} = 18 nm, whereas the smallest observable grains within the matrix of the PSS corresponded to 30 nm.

In contrast to the monomineralic quartzite, the andesite hosted slickenlines exhibit two distinct parts that can be discriminated by a break in the GSD slope. Two D-values are obtained: a lower, $D_{<}$ = *2.05 ± 0.16*, for small grain sizes ($d<d_k$), and $D_{>}$ = *2.68 ± 0.13*, for large grain sizes ($d > d_k$), where $d_{k.}$ *2* µm and is the grain size at the intersection of the two curve fits. Within the small grain size range, the smallest grains are found embedded within the PSS matrix with a d_{min}=30 nm.

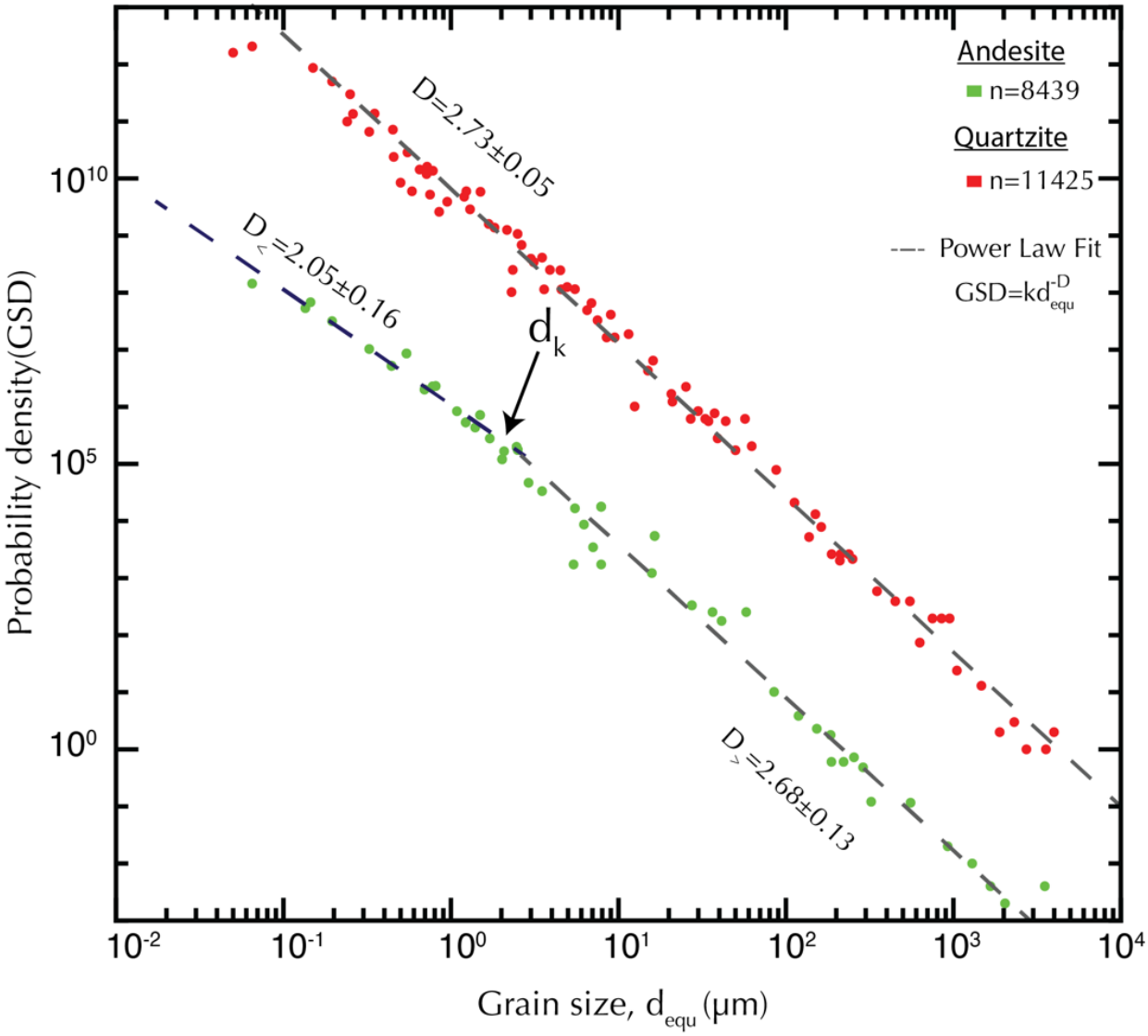

Figure 10. Grain Size Distributions of quartzite (red) and andesite (green) host rocks. Data has been displaced vertically for clarity. Note that GSD of quartzite samples can be described by a single $D = 2.73 \pm 0.05$, whereas GSD has two distinct slopes for $D_< = 2.05 \pm 0.16$ and $D_> = 2.68 \pm 0.13$ for grain size smaller or larger than d_k 2 µm, respectively.

4 Discussion

The results shown in this paper point towards four main observations: 1) regardless of lithology or tectonic setting, individual fault surfaces are self-affine, 2) exhibit a PSZ and PSS, 3) and nanoparticles and potentially amorphous ma-

terial comprise a significant portion of the PSS. In contrast, 4) the grain size distribution within the fault volume appears to be lithology dependent.

The individual samples studied in this project suggest that fault surfaces are self-affine surfaces with Hurst exponents (H) and pre-factors (C) within 0.4-0.8 range and 10^{-5} - $10^{-1,}$ respectively, agreeing with other faults measured in the literature (Bistacchi et al., 2011; Candela et al., 2009, 2012; Power & Tullis, 1989; Thom et al., 2017). Moreover, *smoother* surfaces, generally associated with higher kurtosis and lower skewness, appear to be hosted in more pervasively damaged rocks that likely experienced more slip, further confirming observations on the maturation of fault surfaces with slip (Sagy et al., 2007). Notwithstanding, the results show that measurements from the same locality and even from different portions of the same surface show significant variability in both their H and C, with no systematic trend. Similar variability in the fractal descriptors (H and C) in other measured faults has also been observed in the literature even when such observations are carried out at much longer length scales (tens to hundreds of meters) with the use of *LIDAR* and Photogrammetric Analysis (Bistacchi et al., 2011; Candela et al., 2009, 2012). While the changes in the pre-factor between different scales can be attributed to the measuring device, it can easily be corrected by taking into account the instrument's resolution (Bhushan, 2013; Costa, 2000). The changes observed when measuring different locations of the same surface with the same instrument and at similar scales cannot therefore be easily explained. Thus, suggesting that faults surfaces have inherent local variability in their topography that a) does not follow a simple self-affine model, or b) the current techniques and assumptions used to study fault roughness are not sufficient to fully characterize the intricacy of fault surfaces.

Among some of the intricacies of fault surfaces observed in this study is the presence of a PSZ and PSS in all samples, regardless of lithology. The latter suggests an extreme degree of localization of strain. Most of the deformation is accommodated by grain size reduction along an extremely thin volume of rock, generally a few tens of microns thick, as documented in Fig. 8. Interestingly, the way the grain sizes are distributed appears to vary between the andesite and the quartzite sample. For instance, the slickenline within the quartzite shows a GSD that can be described with a single D value for over six orders of magnitude, whereas the andesite GSD has a break in slope near $d_k = 2$ µm, Fig. 10. Grain size measurements from other polymineralic natural and experimental fault rocks have also reported a break in the slope of their GSD at similar critical grain sizes $\mathrm{d_k}$ (Billi & Storti, 2004; Chester et al., 1993; Chester et al., 2005; Keulen et al., 2007) that suggest a change in the dominant comminution mechanisms with attrition and shearing becoming more important at values lower than d_k. This change, which is not observed in the quartzite sample, could be due to differences in the mechanical properties of the constituent particles becoming more significant as particles approach a critical grain size, wherein the influence of crystal defects decreases with decreasing grain size. Notwithstanding the differences in GSD between the various samples, the abundance of particles in the

nanometer range along faults suggests that grain breakage might be a significant energy sink during fault slip. For instance, Knieke et al. (2009) work on ultrafine particle (nm-range) production with stirred media mills on a variety of different materials shows that the energy required to continue comminuting to ever-smaller particles can be approximated through a power-law. Furthermore, the ultimate size that a particle can be broken into, i.e., grinding limit, depends on a multitude of variables including stressing types, the material of the particles to be milled as well as the size and material of the milling particles, and solvents (e.g., hydrous fluids). Thus, the smallest particles observed along comminuted rocks could reflect the conditions during grinding.

In addition to the extreme grain size reduction, strain localization can also be exhibited via zones of localized amorphization. The material (am?) immediately adjacent to the surface of the slickenline particularly observed in the PP and WH samples, Fig. 9-A-B, E, exhibits a nondescript morphology with no observable grain boundaries suggesting it is likely an amorphous phase. Observation of coeval amorphous and nanocrystalline material has been widely reported along natural fault surfaces (Ault et al., 2019; Houser et al., 2021; Kirkpatrick et al., 2013; Kuo et al., 2016; Ohl et al., 2020; Verberne et al., 2014, 2019; Viti et al., 2016), rock deformation experiments (Kaneki et al., 2020; Marti et al., 2020; Pec et al., 2012, 2016; Pec & Al Nasser, 2021; Toy et al., 2017), and deformation of engineering materials (Han et al., 2012; Viat et al., 2017; Y. S. Zhang et al., 2014; Zhao et al., 2016), indicating that both nanocrystalline and amorphous material are important components during wear processes regardless of the parent material.

4.1 Implications

Fully characterizing a fault surface is of particular importance for better understanding fault processes, as it has been shown that the stress distribution is affected by fault geometry, as the latter controls to a first degree the real contact area (Cattania & Segall, 2021; Harbord et al., 2017; Sagy & Lyakhovsky, 2019). Our current understanding of fault surface geometry is that it is self-affine and that it can be fully characterized by four parameters ($H_{per,}$ $H_{par,}$ $C_{par,}$ C_{per}). While this assumption is useful for making educated predictions of fault surface geometry at scales and locations not currently accessible with the current technology (subsurface faults), our data show that it is not complete. The results shown here suggest that the height distributions of fault surfaces are non-Gaussian. This has important implications on our understanding of fault surface processes, as recent studies in tribology have shown that skewness and kurtosis of the surface height distributions have noticeable effects on surface and frictional properties (e.g., Sedlaček et al., 2012; Tayebi & Polycarpou, 2004; Tomota et al., 2019; S. Zhang et al., 2014).

However, it is worth noting that wear and therefore slip on a fault cannot be entirely described by two rough surfaces sliding past each other, i.e., two body wear (e.g., Bhushan 2013). Instead, observations from natural and synthetic fault surfaces and damage zones suggest that the *surfaces* are, in fact, zones

of extremely localized strain. This is particularly clear when we look at cross-sections of fault surface samples, where we do not observe a single planar surface. Instead, a discrete zone that generally comprises extremely comminuted layers with an abundance of nanoparticles and/or other types of tribofilms, within the PSZ and PSS, is observed (Ault et al., 2019; Brodsky et al., 2020; Dor & Reches, 2005; Goldberg et al., 2016; Heesakkers et al., 2011; Houser et al., 2021; Kuo et al., 2016; Ohl et al., 2020; Pec et al., 2016; William L. Power & Tullis, 1989; Rowe et al., 2019; Siman-Tov et al., 2013, 2015, 2017; Verberne et al., 2014, 2019; Viti et al., 2016). The latter suggests fault surface processes and the evolution of their roughness could be better explained by what is known in tribology as third-body wear, i.e., wear that includes a third particle (or set of particles) that is/are independent of the two rubbing surfaces, as has been recently suggested by (Brodsky et al., 2020) as a way to explain groove generation in fault surfaces as well as the evolution towards self-affine surfaces (Milanese et al., 2019).

5 Summary and Conclusions

We have analyzed slickenline samples from three different fault systems and shown that despite the PSD of each individual sample following a power law, samples from the same fault surface show different fractal parameters suggesting that fault surface topographies do not follow a simple self-affine model. We have also shown that the height distribution of such surfaces are non-Gaussian, and their perceived roughness shows some relation to the strain accumulated in the host rock, with smoother slickenlines accommodating more strain than rougher ones.

Microstructural observations throughout all samples show extreme comminution confined within a small region of the fault rock immediately adjacent to the slip surface wherein nanosized particles are abundant along with other tribofilms and reaction products. The comminution process is marked by a GSD that follows a power law with a fractal dimension $D = 2.73 \pm 0.05$ for quartzite and $D_{<} = 2.05 \pm 0.16$ and $D_{>} = 2.68 \pm 0.13$ with an intersection around d_k 2 µm for andesite. In both cases, for values larger than d_k, the GSD is similar to the D-values predicted by the confined comminution model by Sammis et al. (1987), where grain breakage is controlled by the size of the nearest neighboring grains.

Our observations, therefore suggest that a revision of our assumptions about surface roughness is needed. Furthermore, the prevalence of nanoparticles observed

within fault zones regardless of lithology or tectonic setting urges the need to investigate the processes responsible for their formations, the effect of nanogranular material on the rheological and frictional properties of faults and revise the current assumption for the limits of grinding. In this light, a re-visiting of the energy budget of faulting is necessary to account for the work done to decrease the grain sizes to nanometers. Partitioning of energy between heat, grain breakage, intracrystalline deformation, amorphization, and seismic wave radiation will ultimately influence how much energy goes into heating (Bestmann et al., 2011; Knieke et al., 2009; Ranganathan et al., 2021; Rosakis et al., 2000; Wilson et al., 2005).

6 Acknowledgments

Funding for the CORD technician support from NSF # 1833478 and funding by the J.H. and E.V. Wade Fund from MIT's research support committee is gratefully acknowledged.

We would also like to thank Christie Rowe and McGill University, who allowed us to join their 2019 field course and collect the Waterman Hill samples. The MIT-EAPS 2020 field course for allowing us to collect the Big Piute samples, and Juan Ignacio Arroyo Verástegui, who helped me collect the sample from Falla de Plan de los Plátanos.

Data Availability Statement

Data reported here are publicly available at Zenodo Repository at: https://doi.org/10.5281/zenodo.5176292 (SEM-BSE and petrographic photomicrographs), https://doi.org/10.5281/zenodo.5167913 (surface roughness data), and https://doi.org/10.5281/zenodo.5177184 (grain size distribution data) under a Creative Commons Attribution 4.0 International Public License.

7 References

Ault, A. K., Jensen, J. L., McDermott, R. G., Shen, F.-A., & Van Devener, B. R. (2019). Nanoscale evidence for temperature-induced transient rheology and postseismic fault healing. *Geology*, *47*(12), 1203–1207. https://doi.org/10.1130/G46317.1Bestmann, M., Pennacchioni, G., Frank, G., Göken, M., & de Wall, H. (2011). Pseudotachylyte in muscovite-bearing quartzite: Coseismic friction-induced melting and plastic deformation of quartz. *Journal of Structural Geology*, *33*(2), 169–186. https://doi.org/10.1016/j.jsg.2010.10.009Bhushan, B. (2013). *Introduction to Tribology*. John Wiley & Sons. Retrieved from https://play.google.com/store/books/details?id=b0nhJrqsoZ0CI
A., & Storti, F. (2004). Fractal distribution of particle size in carbonate cataclastic rocks from the core of a regional strike-slip fault zone. *Tectonophysics*, *384*(1),

115–128. https://doi.org/10.1016/j.tecto.2004.03.015Bistacchi, A., Griffith, W. A., Smith, S. A. F., Di Toro, G., Jones, R., & Nielsen, S. (2011). Fault Roughness at Seismogenic Depths from LIDAR and Photogrammetric Analysis. *Pure and Applied Geophysics*, *168*(12), 2345–2363. https://doi.org/10.1007/s00024-011-0301-7Bowden, F. P., Tabor, D., & Taylor, G. I. (1939). The area of contact between stationary and moving surfaces. *Proceedings of the Royal Society of London. Series A, Mathematical and Physical Sciences*, *169*(938), 391–413. https://doi.org/10.1098/rspa.1939.0005Brodsky, E. E., McLaskey, G. C., & Ke, C.-Y. (2020). Groove generation and coalescence on a large-scale laboratory fault. *AGU Advances*, *1*(4). https://doi.org/10.1029/2020av000184Caine, J. S., Evans, J. P., & Forster, C. B. (1996). Fault zone architecture and permeability structure. *Geology*, *24*(11), 1025–1028. https://doi.org/10.1130/0091-7613(1996)024<1025:FZAAPS>2.3.CO;2Candela, T., Renard, F., Bouchon, M., Brouste, A., Marsan, D., Schmittbuhl, J., & Voisin, C. (2009). Characterization of Fault Roughness at Various Scales: Implications of Three-Dimensional High Resolution Topography Measurements. *Pure and Applied Geophysics*, *166*(10), 1817–1851. https://doi.org/10.1007/s00024-009-0521-2Candela, T., Renard, F., Klinger, Y., Mair, K., Schmittbuhl, J., & Brodsky, E. E. (2012). Roughness of fault surfaces over nine decades of length scales. *Journal of Geophysical Research*, *117*(B8). https://doi.org/10.1029/2011jb009041Cattania, C., & Segall, P. (2021). Precursory slow slip and foreshocks on rough faults. *Journal of Geophysical Research, [Solid Earth]*, *126*(4). https://doi.org/10.1029/2020jb020430Chen, J., Verberne, B. A., & Niemeijer, A. R. (2020). Flow-to-Friction Transition in Simulated Calcite Gouge: Experiments and Microphysical Modeling. *Journal of Geophysical Research, [Solid Earth]*, *125*(11), e2020JB019970. https://doi.org/10.1029/2020JB019970Chester, F. M., & Logan, J. M. (1986). Implications for mechanical properties of brittle faults from observations of the Punchbowl fault zone, California. *Pure and Applied Geophysics*, *124*(1), 79–106. https://doi.org/10.1007/BF00875720Chester, Frederick M., Evans, J. P., & Biegel, R. L. (1993). Internal structure and weakening mechanisms of the San Andreas Fault. *Journal of Geophysical Research*, *98*(B1), 771–786. https://doi.org/10.1029/92jb01866Chester, J. S., Chester, F. M., & Kronenberg, A. K. (2005). Fracture surface energy of the Punchbowl fault, San Andreas system. *Nature*, *437*(7055), 133–136. https://doi.org/10.1038/nature03942Childs, C. J., Manzocchi, T., Walsh, J. J., & Schopfer, M. P. J. (2012). Fault core/damage zone; An unhelpful description of fault zone structure? In *3rd EAGE International Conference on Fault and Top Seals*. Netherlands: EAGE Publications BV. https://doi.org/10.3997/2214-4609.20143012Costa, M. A. (2000). *Fractal description of rough surfaces for haptic display* (Doctor of Philosophy). (M. R. Cutkosky, Ed.). Stanford University Stanford, CA. Retrieved from http://www-cdr.stanford.edu/touch/publications/costa_thesis.pdfDe la Teja Segura, M. Á., & Roque Ayala, A. (2007). Carta Geológica-Minera Autlán de Navarro E13-B12 Jalisco. (S. G. Mexicano, Ed.). Pachuca, HGO, Mexico : Servicio Geológico Mexicano. Retrieved from http://mapserver.sgm.gob.mx/Cartas_Online/geologia/956_E13-

B12_GM.pdfDi Toro, G., Han, R., Hirose, T., De Paola, N., Nielsen, S., Mizoguchi, K., et al. (2011). Fault lubrication during earthquakes. *Nature*, *471*(7339), 494–498. https://doi.org/10.1038/nature09838Dieterich, J. H., & Kilgore, B. D. (1996). Imaging surface contacts: power law contact distributions and contact stresses in quartz, calcite, glass and acrylic plastic. *Tectonophysics*, *256*(1), 219–239. https://doi.org/10.1016/0040-1951(95)00165-4Doblas, M. (1998). Slickenside kinematic indicators. *Tectonophysics*, *295*(1), 187–197. https://doi.org/10.1016/S0040-1951(98)00120-6Dor, O., & Reches, Z. (2005). *Analysis of Fault Zones Associated with Large Earthquakes in South African Gold Mines*. Earth Sciences Institute, Hebrew University, Jerusalem, Israel. Retrieved from http://earthquakes.ou.edu/nelsam/fault_zones.pdfvan den Ende, M. P. A., Chen, J., Ampuero, J.-P., & Niemeijer, A. R. (2018). A comparison between rate-and-state friction and microphysical models, based on numerical simulations of fault slip. *Tectonophysics*, *733*, 273–295. https://doi.org/10.1016/j.tecto.2017.11.040Faulkner, D. R., Jackson, C. A. L., Lunn, R. J., Schlische, R. W., Shipton, Z. K., Wibberley, C. A. J., & Withjack, M. O. (2010). A review of recent developments concerning the structure, mechanics and fluid flow properties of fault zones. *Journal of Structural Geology*, *32*(11), 1557–1575. https://doi.org/10.1016/j.jsg.2010.06.009Faulkner, D. R., Mitchell, T. M., Jensen, E., & Cembrano, J. (2011). Scaling of fault damage zones with displacement and the implications for fault growth processes. *Journal of Geophysical Research*, *116*(B5). https://doi.org/10.1029/2010jb007788Fletcher, J. M., Bendixen, J., Fillmore, R., Walker, J. D., Glazner, A. F., & Bartley, J. M. (1999). Geology of the Mitchel Range and Waterman Hills, San Bernardino County, California. Geological society of America. https://doi.org/10.1130/1999-fletcher-watermanhillsFleuty, M. J. (1975). Slickensides and slickenlines. *Geological Magazine*, *112*(3), 319–322. https://doi.org/10.1017/S0016756800047087Goldberg, R., Siman-Tov, S., & Emmanuel, S. (2016). Weathering resistance of carbonate fault mirrors promotes rupture localization. *Geophysical Research Letters*. https://doi.org/10.1002/2016gl067788Han, S., Zhao, L., Jiang, Q., & Lian, J. (2012). Deformation-induced localized solid-state amorphization in nanocrystalline nickel. *Scientific Reports*, *2*, 493. https://doi.org/10.1038/srep00493Harbord, C. W. A., Nielsen, S. B., De Paola, N., & Holdsworth, R. E. (2017). Earthquake nucleation on rough faults. *Geology*, *45*(10), 931–934. https://doi.org/10.1130/G39181.1Heesakkers, V., Murphy, S., & Reches, Z. (2011). Earthquake Rupture at Focal Depth, Part I: Structure and Rupture of the Pretorius Fault, TauTona Mine, South Africa. *Pure and Applied Geophysics*, *168*(12), 2395–2425. https://doi.org/10.1007/s00024-011-0354-7Houser, L. M., Ault, A. K., Newell, D. L., Evans, J. P., Shen, F.-A., & Van Devener, B. R. (2021). Nanoscale textural and chemical evolution of silica fault mirrors in the Wasatch fault damage zone, Utah, USA. *Geochemistry, Geophysics, Geosystems*, *22*(3). https://doi.org/10.1029/2020gc009368Jacobs, T. D. B., Junge, T., & Pastewka, L. (2017). Quantitative characterization of surface topography using spectral analysis. *Surface Topography: Metrology and Properties*,

5(1), 013001. https://doi.org/10.1088/2051-672X/aa51f8Kaneki, S., Oohashi, K., Hirono, T., & Noda, H. (2020). Mechanical amorphization of synthetic fault gouges during rotary-shear friction experiments at subseismic to seismic slip velocities. *Journal of Geophysical Research, [Solid Earth]*, *125*(10). https://doi.org/10.1029/2020jb019956Keulen, N., Heilbronner, R., Stünitz, H., Boullier, A.-M., & Ito, H. (2007). Grain size distributions of fault rocks: A comparison between experimentally and naturally deformed granitoids. *Journal of Structural Geology*, *29*(8), 1282–1300. https://doi.org/10.1016/j.jsg.2007.04.003Kim, Y.-S., Peacock, D. C. P., & Sanderson, D. J. (2004). Fault damage zones. *Journal of Structural Geology*, *26*(3), 503–517. https://doi.org/10.1016/j.jsg.2003.08.002Kirkpatrick, J. D., Rowe, C. D., White, J. C., & Brodsky, E. E. (2013). Silica gel formation during fault slip: Evidence from the rock record. *Geology*, *41*(9), 1015–1018. https://doi.org/10.1130/G34483.1Knieke, C., Sommer, M., & Peukert, W. (2009). Identifying the apparent and true grinding limit. *Powder Technology*, *195*(1), 25–30. https://doi.org/10.1016/j.powtec.2009.05.007Kuo, L.-W., Song, S.-R., Suppe, J., & Yeh, E.-C. (2016). Fault mirrors in seismically active fault zones: A fossil of small earthquakes at shallow depths. *Geophysical Research Letters*, *43*(5), 1950–1959. https://doi.org/10.1002/2015gl066882Magloughlin, J. F., & Spray, J. G. (1992). Frictional melting processes and products in geological materials: introduction and discussion. *Tectonophysics*, *204*(3), 197–204. https://doi.org/10.1016/0040-1951(92)90307-RMandelbrot, B. B. (1985). Self-Affine Fractals and Fractal Dimension. *Physica Scripta*, *32*(4), 257. https://doi.org/10.1088/0031-8949/32/4/001Marti, S., Stünitz, H., Heilbronner, R., & Plümper, O. (2020). Amorphous material in experimentally deformed mafic rock and its temperature dependence: Implications for fault rheology during aseismic creep and seismic rupture. *Journal of Structural Geology*, *138*, 104081. https://doi.org/10.1016/j.jsg.2020.104081Milanese, E., Brink, T., Aghababaei, R., & Molinari, J.-F. (2019). Emergence of self-affine surfaces during adhesive wear. *Nature Communications*, *10*(1), 1116. https://doi.org/10.1038/s41467-019-09127-8Nielsen, S., Mosca, P., Giberti, G., Di Toro, G., Hirose, T., & Shimamoto, T. (2010). On the transient behavior of frictional melt during seismic slip. *Journal of Geophysical Research*, *115*(B10). https://doi.org/10.1029/2009jb007020Ohl, M., Plümper, O., Chatzaras, V., Wallis, D., Vollmer, C., & Drury, M. (2020). Mechanisms of fault mirror formation and fault healing in carbonate rocks. *Earth and Planetary Science Letters*, *530*, 115886. https://doi.org/10.1016/j.epsl.2019.115886Pec, M., & Al Nasser, S. (2021). Formation of nanocrystalline and amorphous materials causes parallel brittle-viscous flow of crustal rocks: Experiments on quartz-feldspar aggregates. *Journal of Geophysical Research, [Solid Earth]*, *126*(5). https://doi.org/10.1029/2020jb021262Pec, M., Stünitz, H., Heilbronner, R., Drury, M., & de Capitani, C. (2012). Origin of pseudotachylites in slow creep experiments. *Earth and Planetary Science Letters*, *355–356*, 299–310. https://doi.org/10.1016/j.epsl.2012.09.004Pec, M., Stünitz, H., Heilbronner, R., & Drury, M. (2016). Semi-brittle flow of granitoid fault rocks in experiments. *Journal of Geophysical Research, [Solid Earth]*, *121*(3), 1677–1705.

https://doi.org/10.1002/2015jb012513Petit, J. P. (1987). Criteria for the sense of movement on fault surfaces in brittle rocks. *Journal of Structural Geology*, *9*(5), 597–608. https://doi.org/10.1016/0191-8141(87)90145-3Power, W. L., Tullis, T. E., Brown, S. R., Boitnott, G. N., & Scholz, C. H. (1987). Roughness of natural fault surfaces. *Geophysical Research Letters*, *14*(1), 29–32. https://doi.org/10.1029/gl014i001p00029Power, William L., & Tullis, T. E. (1989). The relationship between slickenside surfaces in fine-grained quartz and the seismic cycle. *Journal of Structural Geology*, *11*(7), 879–893. https://doi.org/10.1016/0191-8141(89)90105-3Ranganathan, M., Minchew, B., Meyer, C. R., & Pec, M. (2021, July 29). *Deformational-energy partitioning in glacier shear zones. Earth and Space Science Open Archive*. Earth and Space Science Open Archive. https://doi.org/10.1002/essoar.10507633.1Rosakis, P., Rosakis, A. J., Ravichandran, G., & Hodowany, J. (2000). A thermodynamic internal variable model for the partition of plastic work into heat and stored energy in metals. *Journal of the Mechanics and Physics of Solids*, *48*(3), 581–607. https://doi.org/10.1016/S0022-5096(99)00048-4Rowe, C. D., Lamothe, K., Rempe, M., Andrews, M., Mitchell, T. M., Di Toro, G., et al. (2019). Earthquake lubrication and healing explained by amorphous nanosilica. *Nature Communications*, *10*(1), 320. https://doi.org/10.1038/s41467-018-08238-ySagy, A., & Lyakhovsky, V. (2019). Stress patterns and failure around rough interlocked fault surface. *Journal of Geophysical Research, [Solid Earth]*, *124*(7), 7138–7154. https://doi.org/10.1029/2018jb017006Sagy, A., Brodsky, E. E., & Axen, G. J. (2007). Evolution of fault-surface roughness with slip. *Geology*, *35*(3), 283–286. https://doi.org/10.1130/G23235A.1Sammis, C., King, G., & Biegel, R. (1987). The kinematics of gouge deformation. *Pure and Applied Geophysics*, *125*(5), 777–812. https://doi.org/10.1007/BF00878033Scholz, C. H. (2019). *The Mechanics of Earthquakes and Faulting* (3rd ed.). Cambridge: Cambridge University Press. https://doi.org/10.1017/9781316681473Sedlaček, M., Podgornik, B., & Vižintin, J. (2012). Correlation between standard roughness parameters skewness and kurtosis and tribological behaviour of contact surfaces. *Tribology International*, *48*, 102–112. https://doi.org/10.1016/j.triboint.2011.11.008Shipton, Z. K., Soden, A., Kirkpatrick, J. D., & Lunn, R. (2006). How Thick is a Fault? Fault Displacement-Thickness Scaling Revisited. *Geophysical Monograph Series*, *170*. https://doi.org/10.1029/170GM19Siman-Tov, S., Aharonov, E., Sagy, A., & Emmanuel, S. (2013). Nanograins form carbonate fault mirrors. *Geology*, *41*(6), 703–706. https://doi.org/10.1130/G34087.1Siman-Tov, S., Aharonov, E., Boneh, Y., & Reches, Z. (2015). Fault mirrors along carbonate faults: Formation and destruction during shear experiments. *Earth and Planetary Science Letters*, *430*, 367–376. https://doi.org/10.1016/j.epsl.2015.08.031Siman-Tov, S., Stock, G. M., Brodsky, E. E., & White, J. C. (2017). The coating layer of glacial polish. *Geology*, *45*(11), 987–990. https://doi.org/10.1130/G39281.1Spray, J. G. (1992). A physical basis for the frictional melting of some rock-forming minerals. *Tectonophysics*, *204*(3), 205–221. https://doi.org/10.1016/0040-1951(92)90308-STayebi, N., & Polycarpou, A. A. (2004). Modeling the effect of skewness and kurtosis on the static friction coefficient of rough surfaces. *Tribology International*, *37*(6), 491–505. https://doi.org/10.1016/j.triboint.2003.11.010Thom,

C. A., Brodsky, E. E., Carpick, R. W., Pharr, G. M., Oliver, W. C., & Goldsby, D. L. (2017). Nanoscale roughness of natural fault surfaces controlled by scale-dependent yield strength. *Geophysical Research Letters*, *44*(18), 9299–9307. https://doi.org/10.1002/2017gl074663Tikoff, B., Chatzaras, V., Newman, J., & Roberts, N. M. (2019). Big data in microstructure analysis: Building a universal orientation system for thin sections. *Journal of Structural Geology*, *125*, 226–234. https://doi.org/10.1016/j.jsg.2018.09.019Tisato, N., Di Toro, G., De Rossi, N., Quaresimin, M., & Candela, T. (2012). Experimental investigation of flash weakening in limestone. *Journal of Structural Geology*, *38*, 183–199. https://doi.org/10.1016/j.jsg.2011.11.017Tomota, T., Kondoh, Y., & Ohmori, T. (2019). Modeling Solid Contact between Smooth and Rough Surfaces with Non-Gaussian Distributions. *Tribology Transactions*, *62*(4), 580–591. https://doi.org/10.1080/10402004.2019.1573341Toy, V. G., Niemeijer, A., Renard, F., Morales, L., & Wirth, R. (2017). Striation and slickenline development on quartz fault surfaces at crustal conditions: Origin and effect on friction. *Journal of Geophysical Research, [Solid Earth]*, *122*(5), 3497–3512. https://doi.org/10.1002/2016jb013498Verberne, B. A., Plümper, O., de Winter, D. A. M., & Spiers, C. J. (2014). Rock mechanics. Superplastic nanofibrous slip zones control seismogenic fault friction. *Science*, *346*(6215), 1342–1344. https://doi.org/10.1126/science.1259003Verberne, B. A., Plümper, O., & Spiers, C. J. (2019). Nanocrystalline Principal Slip Zones and Their Role in Controlling Crustal Fault Rheology. *Minerals*, *9*(6), 328. https://doi.org/10.3390/min9060328Viat, A., Guillonneau, G., Fouvry, S., Kermouche, G., Sao Joao, S., Wehrs, J., et al. (2017). Brittle to ductile transition of tribomaterial in relation to wear response at high temperatures. *Wear: An International Journal on the Science and Technology of Friction Lubrication and Wear*, *392–393*, 60–68. https://doi.org/10.1016/j.wear.2017.09.015Viti, C., Brogi, A., Liotta, D., Mugnaioli, E., Spiess, R., Dini, A., et al. (2016). Seismic slip recorded in tourmaline fault mirrors from Elba Island (Italy). *Journal of Structural Geology*, *86*, 1–12. https://doi.org/10.1016/j.jsg.2016.02.013Wilson, B., Dewers, T., Reches, Z., & Brune, J. (2005). Particle size and energetics of gouge from earthquake rupture zones. *Nature*, *434*(7034), 749–752. https://doi.org/10.1038/nature03433Zhang, S., Wang, W., & Zhao, Z. (2014). The effect of surface roughness characteristics on the elastic–plastic contact performance. *Tribology International*, *79*, 59–73. https://doi.org/10.1016/j.triboint.2014.05.016Zhang, Y. S., Zhang, L. C., Niu, H. Z., Bai, X. F., Yu, S., Ma, X. Q., & Yu, Z. T. (2014). Deformation twinning and localized amorphization in nanocrystalline tantalum induced by sliding friction. *Materials Letters*, *127*, 4–7. https://doi.org/10.1016/j.matlet.2014.04.079Zhao, S., Hahn, E. N., Kad, B., Remington, B. A., Wehrenberg, C. E., Bringa, E. M., & Meyers, M. A. (2016). Amorphization and nanocrystallization of silicon under shock compression. *Acta Materialia*, *103*, 519–533. https://doi.org/10.1016/j.actamat.2015.09.022